Spectroscopy of Cold, Trapped Atoms

Tomasz M. Brzozowski,[@] Maria Brzozowska, Jerzy Zachorowski
and Wojciech Gawlik

Marian Smoluchowski Institute of Physics, Jagiellonian University
30-059 Cracow, Poland

[@] Corresponding author; E-mail: tmb@ceti.pl

Abstract. We describe the results of the pump-probe spectroscopy performed with ^{85}Rb atoms trapped in a magneto-optical trap (MOT). We show how various processes associated with light–atom interactions shape the observed spectra and how their features can be utilized for obtaining information about properties of cold-atom sample. In particular, we emphasize the important role of the atomic-recoil phenomenon and use it for efficient and reliable velocimetry of the working MOT.

Keywords: nonlinear optics, spectroscopy, cold atoms
PACS: 32.80.Pj, 42.50.Vk, 42.65.-k

1. Introduction

Cold atomic samples constitute a convenient medium for studying light–matter interaction. Due to significantly reduced Doppler broadening, low collision rate and long interaction time, such samples offer a unique possibility of precision spectroscopic measurements, being especially useful for experiments which investigate Raman transitions between nearly degenerate energy levels. It should be noted that the described experiments probe both the internal state of an atom (excitations) as well as the external degrees of freedom (motion of the whole atom). The resonant structures in probe spectra observed in cold media for pump-probe detuning much smaller than the natural linewidth are due to numerous effects: stimulated Rayleigh scattering [1] and Raman transitions between either light shifted sublevels of a ground atomic state (Raman–Zeeman Resonances, RZR) [2,3], vibrational energy levels of atoms localized in an optical lattice (Raman-Vibrational Resonances, RVR) [4], or kinetic momentum states of unbound atoms (Recoil-Induced Resonances, RIR) [5–7].

The magneto-optical trap (MOT) while being a standard tool for obtaining cold atomic samples, does not provide ideal environment for systematic investigation of these effects. Because of the fixed three-dimensional geometry of the trapping beams, presence of inhomogeneous trapping field, and limited flexibility in varying the trap parameters, it is difficult to selectively address the phenomena mentioned above. This is why the MOT usually serves only as an initial stage of preparation of a cold sample which, after switching off the MOT's optical and magnetic fields, is subject to more precisely controlled experimental conditions, such as dedicated pump beam geometry and polarization [1, 5, 8–10], phase-stabilized pump beams [11], etc.

Despite these difficulties, several authors have studied cw pump-probe spectroscopy of trapped atoms performed while the MOT is working with the trapping beams acting as pump light. Such experiments were first carried out by Tabosa et al. [12] and Grison et al. [2]. Also, spectroscopic evidence of optical lattices in a MOT with a special, phase-shift-insensitive, trapping beam geometry has been reported [13, 7]. These experiments indicated potential of the probe spectroscopy for cold-atom diagnostics. However, the complexity of such spectra from a working MOT limited their possible application for MOT diagnostics. In this paper we revisit the problem, describe our systematic studies of such spectra and present a novel method of extending standard Raman MOT spectroscopy by introduction of an extra, far-detuned pump beam. Such an approach resulted in much desired uncoupling of the probe spectra from the trapping beam parameters, full isolation of the RIR and creation of the robust 1D optical lattices superimposed on the cloud of cold, trapped atoms. One important consequence was application of the RIRs for non-destructive diagnostics of a working trap.

This article in organized as follows. In Sec. 2 we briefly discuss the probe absorption and four-wave mixing spectra when probe beam frequency is scanned in a relatively wide range around frequency of the trapping beams. In Sec. 3 we concentrate on the central structure of the spectra discussed in Sec. 2 and interpret them as a result of Raman transitions between discrete light-shifted Zeeman atomic sublevels and momentum states in the continuum of kinetic energy. In Sec. 4 we show that these latter transitions, responsible for recoil-induced resonances can be used for non-destructive diagnostics of the cold atomic sample practically of any kind (MOT, optical molasses, optical lattices). Sec. 5 concludes the paper.

2. Probe Absorption and Four-Wave Mixing in a MOT

2.1. Experimental setup

We use a standard vapor-loaded magneto-optical trap [14]. Our laser setup consists of four home-built diode lasers. One of them, equipped with an external cavity, is frequency stabilized using saturated absorption in a rubidium vapor cell. This laser serves as the master for injection seeding into the trapping and probe lasers. The 780 nm light from a 70-mW trapping diode laser is divided into three beams, which

have Gaussian radii $\sigma \approx 0.4$ cm and peak intensities $I_{max} = 20$ mW/cm^2 in the MOT cell. They are retro-reflected after passing the trap cell and $\lambda/4$ plates. The frequency shift of the trapping and probe beams is controlled by several acousto-optic modulators (AOMs). The typical detuning of the trapping beam frequency ω from the trapping resonance frequency ω_0, $\Delta = \omega - \omega_0 = -3\Gamma$, where $\Gamma = 2\pi \times 5.98$ MHz is the transition's natural linewidth. Before injection into the probe laser diode the master beam double passes the AOM, which allows us to tune the frequency ω_{pr} of the probe laser in the range of ± 40 MHz around the master laser frequency. Since both trapping and probe lasers are seeded with the same beam, their phase fluctuations are correlated. Thus, when these two lasers work in the pump-probe Raman configuration they provide a spectroscopic resolution which allows one to distinguish resonant structures with widths of a few kHz, limited by residual phase fluctuations. The repumping beam is derived from an independent, free running laser diode, and is overlapped with one of the trapping beams. The quadrupole magnetic field is generated by a pair of anti-Helmholtz coils, which produce an axial gradient of 16 G/cm. Stray dc magnetic fields are zeroed by three orthogonal pairs of Helmholtz coils. We trap about 10^7 atoms in the cloud with a Gaussian radius of $\sigma \approx 0.9$ mm. The temperature of our sample stays in the 10–200 μK range, depending on the trapping conditions.
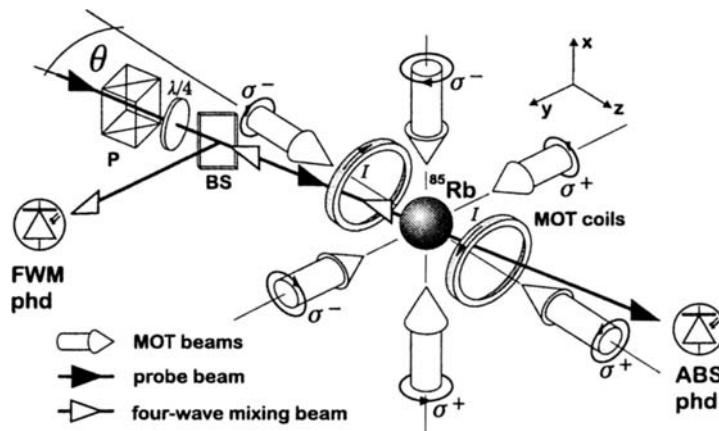

Fig. 1. The geometry of the experimental setup

The geometry of our experiment is depicted in Fig. 1. The probe beam enters the cloud of cold atoms making a small angle $\theta = 3.5°$ with one of the trapping beams. The probe beam polarization is set by a $\lambda/4$ waveplate placed after a polarizer (P). The polarization is defined the with respect to the nearest, nearly co-propagating trapping beam, which is σ^--polarized. We call the probe polarization σ^- (σ^+) when it is the same as that of the nearly co-propagating (counter-propagating) trapping beam. After traversing the cloud, the probe beam is directed

onto a photodiode which records the absorption spectrum (ABS phd). The four-wave mixing beam, generated in the cloud and propagating oppositely to the probe beam, is reflected by a 50/50 beamsplitter (BS) onto another photodiode (FWM phd). Both signals are acquired simultaneously and thus can be directly compared. The probe beam is shaped to have its diameter smaller than the cloud size in order to avoid undesired background of non-absorbed light. Typically, the probe-laser power is about 1 μW and its frequency is swept at a rate of 5 MHz/s. The spectra presented in this paper are recorded as a function of the pump-probe detuning, $\delta = \omega_{\mathrm{pr}} - \omega$. and are typically averaged over 20 probe sweeps.

2.2. Results

The example of the probe absorption and four-wave mixing spectra recorded in the setup discussed above is presented in Fig. 2. Both spectra exhibit a characteristic
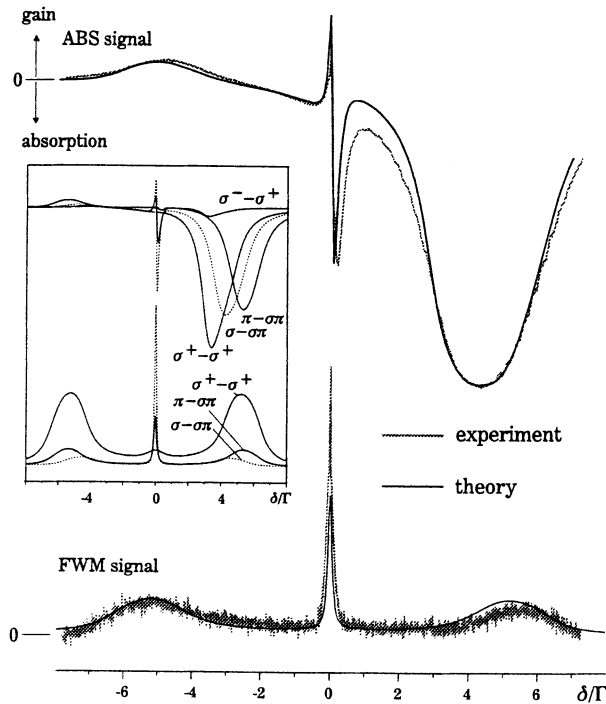

Fig. 2. Experimental absorption (ABS) and four-wave mixing (FWM) spectra (grey lines) and their theoretical modeling (black lines). Inset shows contributions of three different pump-probe polarization configurations used to model the experimental data (the first symbol denotes probe beam polarization, the second — net polarization of the pump field). Experimental conditions: $I = 10.4$ mW/cm^2 per beam. σ^--polarized probe beam, axial magnetic field gradient $\partial B/\partial z = 13$ Gauss/cm. $\Delta = -3\Gamma$

structure: they comprise narrow, central resonance for pump-probe detuning $\delta \approx 0$ and two sideband resonances. Such a shape can be qualitatively understood in terms of a two-level dressed atom [15]. As depicted in Fig. 3a, photons from the pump beam of frequency ω interact with a two-level atom of resonant frequency ω_0, which leads to energy level splitting. Both ground $|g\rangle$ and excited $|e\rangle$ atomic levels are split into two dressed states separated by Ω', where Ω' denotes the generalized Rabi frequency [15]. When such a structure is probed with the laser of tunable frequency ω_{pr}, three distinct resonances arise (Fig. 3b): one at $\omega_{pr} = \omega$ and two other at $\omega_{pr} = \omega \pm \Omega'$. In the case of absorption, the resonance at $\omega_{pr} = \omega$ exhibits a
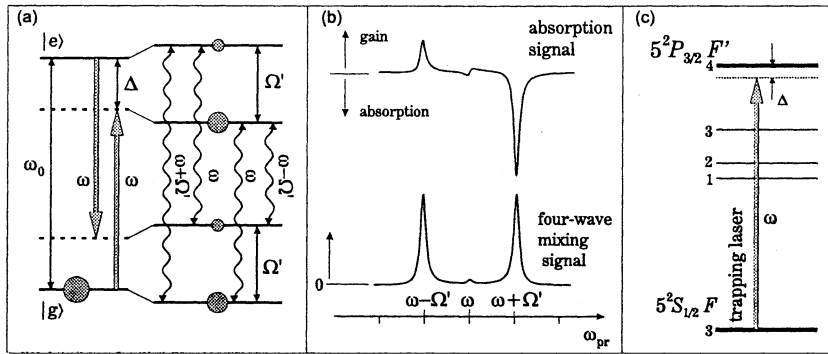

Fig. 3. (a) Two-level atom dressed by photons of monochromatic laser field of frequency ω, red-detuned by δ from atomic transition frequency ω_0. Wavy arrows indicate possible transitions between dressed levels, sizes of the grey circles symbolize populations of the respective levels. (b) Absorption and four-wave mixing spectra as a function of the probe beam detuning, ω_{pr}. (c) Real situation: multilevel structure of the ^{85}Rb atoms dressed by the intensity- and polarization-modulated trapping field of frequency ω

dispersive shape, while resonances at $\omega_{pr} = \omega \pm \Omega'$ are associated with attenuation and amplification of the probe beam, respectively. In the case of the four-wave mixing process which results in the generation of the fourth-wave photon every time the resonance condition is fulfilled, all three resonances are positive peaks, associated with emission of photons in the fourth-wave propagation direction. Although the spectra in Fig. 2 exhibit all the listed features, they essentially differ from the predictions of a simple model of the two level atom dressed by monochromatic photons. The ^{85}Rb atoms in a magneto-optical trap cannot, in general, be treated in the two-level approximation. They exhibit a multilevel structure and interact with an intense trapping field (Fig. 3c) which, as a result of the interference of the six $\sigma^{\pm}$-polarized trapping beams, becomes strongly inhomogeneous. Depending on its position, an atom sees different polarization and intensity of the pump field and the probe beam. Hence, in order to model the resultant spectra one has to average the calculated spectra over a wide range of Rabi frequencies and polarization

configurations. Results of such a numerical modeling based on master equation [16] for the $F = 3 \rightarrow F' = 4$ transition and for various probe and pump beam polarizations is depicted in Fig. 2. If we take a closer look at the resonance at
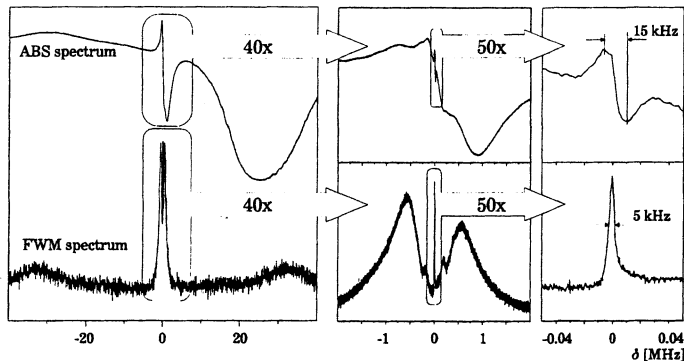

Fig. 4. The central resonance at $\delta \simeq 0$ in the probe absorption and four-wave mixing spectra in a magneto-optical trap develops complex structure, as revealed by subsequent narrowings of the probe frequency sweep range. The signals in the first column are mainly due to optical transitions between the dressed atomic levels. The resonances plotted in the second and third columns are associated with the Raman transitions: between light-shifted Zeeman sublevels of the ground atomic state (second column) and between kinetic momentum states (third column)

$\omega_{\text{pr}} \simeq \omega$ (for $\delta \simeq 0$) by subsequent narrowing of the probe frequency range, we will see that it comprises many different contributions (Fig. 4). They originate from Raman transitions and will be discussed in the next section.

3. Central Resonant Structure: Raman–Zeeman and Recoil-Induced Resonances

To understand the origin of the central resonant structure we employ the idea of Raman transitions depicted schematically in Fig. 5. Two atomic levels, $|1\rangle$ and $|2\rangle$, separated by energy $\hbar\delta_{21}$, are subject to two laser fields of frequencies ω_1 and ω_2. If frequencies of these fields are chosen so that $\omega_2 - \omega_1 = \delta_{21}$, the two-photon transition between $|1\rangle$ and $|2\rangle$ via level $|v\rangle$ becomes possible and the resonance occurs with the absorption of a photon from one beam and emission of a photon to the other beam. The direction of the process (from $|1\rangle$ to $|2\rangle$ or vice versa) is governed by the initial population of the levels — the process starting from the more populated level outweighs the reverse one, hence the signal amplitude is proportional to the population difference of states $|1\rangle$ and $|2\rangle$. The discussed process occurs even if $|v\rangle$ is a virtual state.
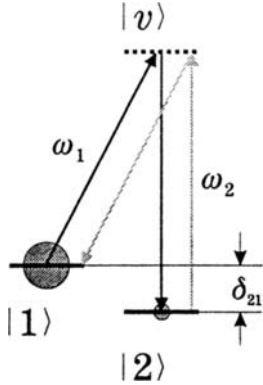
Fig. 5. Raman transition between atomic levels $|1\rangle$ and $|2\rangle$ (via level $|v\rangle$, which can be virtual), separated by energy $\hbar\delta_{21}$, induced by two laser beams of frequencies ω_1 and ω_2, occurs when the resonance condition $\omega_2 - \omega_1 = \delta_{21}$ is fulfilled. The direction and the amplitude of the process are governed by the population difference. The process starting from more populated level (black arrows) predominates the reverse one (grey arrows)

In the conditions of our experiment, the shape of the central resonance in the absorption and four-wave mixing spectra can be explained on the basis of two processes: Raman transitions between light-shifted Zeeman sublevels of the ground state yielding the Raman–Zeeman resonances [2,17] and recoil-induced resonances (RIR) [5]. Theoretical outline of both processes is presented below.

3.1. Raman transitions between light-shifted Zeeman sublevels (RZR)

Let us consider the cycling transition in the ^{85}Rb atom, $5\,^2S_{1/2}$ $(F_g = 3) - 5\,^2P_{3/2}$ $(F_e = 4)$. The atom in a MOT is subject to three pairs of counter-propagating laser beams of frequency ω with pairwise orthogonal circular polarizations. As mentioned before, their interference in the intersection region results in a complex spatial modulation of light intensity and polarization [18]. For the sake of simplicity, we consider here only the case where the net light field is linearly polarized and choose quantization axis parallel to the local direction of the net field **E**. In this reference frame, the resulting pump light is π-polarized and shifts the Zeeman sublevels of both the ground and the excited atomic state.

The $5\,^2S_{1/2}$ $(F_g = 3)$ ground state multilevel structure is presented in Fig. 6a. The optical pumping in such a scheme leads to distribution of populations which is symmetric with respect to the m_g quantum number, with $m_g = 0$ sublevel being most populated. The atoms interacting with the pump light are probed by a circularly polarized weak probe laser. The Raman processes involving a π-polarized pump and a $\sigma^{\pm}$-polarized probe photon lead to transitions with $\Delta m_g = \pm 1$. For a given population distribution among the m_g sublevels, two directions of such processes are possible, depending on the sign of the probe-pump detuning δ. In the considered case of dominant population in the $m_g = 0$ sublevel, the Raman transitions with $\Delta m = -1$ take place for $\delta < 0$ and lead the probe gain; those with $\Delta m = +1$ take place for $\delta > 0$ and result in its attenuation. These processes are resonant whenever $|\delta|$ coincides with the energy separation of the adjacent sublevels. The amplitude of the corresponding resonance is proportional to the population difference of the sublevels involved in the transition and depends on the Clebsch–
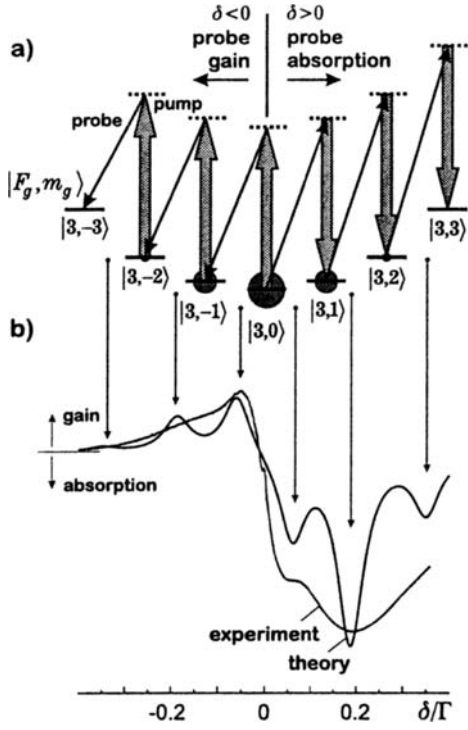
Fig. 6. a) Multilevel structure of the 5 $^2S_{1/2}$ ($F = 3$) ^{85}Rb ground state. Zeeman sublevels are perturbed with a π-polarized pump (thick grey arrows), which results in their energy shift and symmetric population distribution (alignment), marked by grey circles. The structure is then probed by a σ^+-polarized beam. b) Theoretical absorption signal compared with the experimental spectrum. The theoretical curve was generated for the Rabi frequency $\Omega = 6\Gamma$, detuning $\Delta = -3\Gamma$ and $\gamma_{i,k} = 0.13\Gamma$ for all i, k. Experimental conditions: $I_{max} = 10.2$ mW/cm^2, $\Delta = -3\Gamma$, $\partial B/\partial z = 13$ G/cm

Gordan coefficients associated with the specific transition path. The simplest model of the probe absorption spectrum is obtained by summing the Lorentzian profiles centered at the appropriate resonance frequencies and weighted by products of the relevant population differences and squares of the Clebsch–Gordan coefficients

$$s_{\mathrm{RZR}}(\delta) = \sum_{i=1}^{3} w_{i-1,i}\Delta\Pi_{i-1,i}L\left(\delta, \delta_{i-1,i}, \gamma_{i-1,i}\right)$$

$$- \sum_{i=-1}^{-3} w_{i+1,i}\Delta\Pi_{i+1,i}L\left(\delta, \delta_{i+1,i}, \gamma_{i+1,i}\right). \tag{1}$$

In the above equation, $w_{k,j}$ is the weight associated with the Clebsch–Gordan coefficient along the $k = m_g \leftrightarrow j = m_g$ Raman transition path, $\Delta\Pi_{k,j}$ is the population difference of the $k = m_g$ and $j = m_g$ sublevels, and the Lorentzian profile is given by

$$L\left(\delta, \delta_{k,j}, \gamma_{k,j}\right) = \frac{\gamma_{k,j}}{\gamma_{k,j}^2 + (\delta - \delta_{k,j})^2}, \tag{2}$$

where $\delta_{k,j}$ and $\gamma_{k,j}$ are, respectively, the resonance frequencies and widths of the $k = m_g \leftrightarrow j = m_g$ transitions. These widths reflect the optical pumping time,

the finite interaction time and the rate atomic collisions in a trap. The spectrum generated using formula (1) for the closed non-relaxing system shown in Fig. 6a is presented in Fig. 6b and compared to the relevant experimental data. The comparison shows that the latter constitutes an envelope for the theoretical spectrum where individual resonances appear unrealistically well resolved. This suggests a broadening mechanism which is indeed provided by the spatial inhomogeneity of the light intensity in the trap. To account for this effect, we averaged the calculated spectra over Rabi frequency Ω. By numerical simulations of various field contributions, similar to that of Ref. [18], we have found that the relevant range that produces the best agreement between the theory and the experiment is 5Γ to 7.5Γ. This corresponds to the average Rabi frequency of 6.25Γ determined as in Ref. [19]. Accounting for the **E**-field inhomogeneity yields a better agreement of theoretical results with the experimental data. However, there is still a discrepancy between the theoretical prediction and the experimental signal near $\delta \simeq 0$. Moreover, the model discussed above does not explain the profound difference between the spectra registered for σ^+- and σ^--polarized probe. The explanation of this effect is presented in the next subsection.

3.2. Recoil-induced resonances (RIR)

The momentum exchange between non-localized atoms and the laser field is associated with the phenomenon of the so-called recoil-induced resonances (RIR). They were predicted by Guo et al. [20] and observed by Grynberg et al. [5,8]. A simple momentum-space analysis of RIR can be found in Refs. [5,21,22]. Here we briefly recall their results.

Let us consider atoms of mass m interacting with a weak probe beam (with wave vector $\mathbf{k}_{pr}$ and frequency $\omega + \delta$), which makes an angle θ with the direction of propagation of a strong pump beam (wave vector $\mathbf{k}$, frequency ω), as depicted in Fig. 7a. The process of pump photon absorption followed by the probe photon emission results in the momentum change Δp of an atom, where

$$\Delta p = -2\hbar k \sin\frac{\theta}{2} \,. \tag{3}$$

The preceding equation is derived assuming a small probe-pump detuning, $|\mathbf{k}| \approx |\mathbf{k}_{pr}| = k$. The resonance occurs whenever the probe-pump detuning coincides with the kinetic energy difference, namely at detuning

$$\delta_{\text{res}} = -\frac{2k}{m}\left(\hbar k \sin\frac{\theta}{2} - p\right)\sin\frac{\theta}{2} \,. \tag{4}$$

Analogous consideration performed for the case of probe-photon absorption followed by emission of a photon into the pump beam leads to the nearly identical formula for δ_{res} as (4), but with the opposite sign. Similarly to the RZR case, the resonance amplitude is proportional to the population difference between the relevant atomic
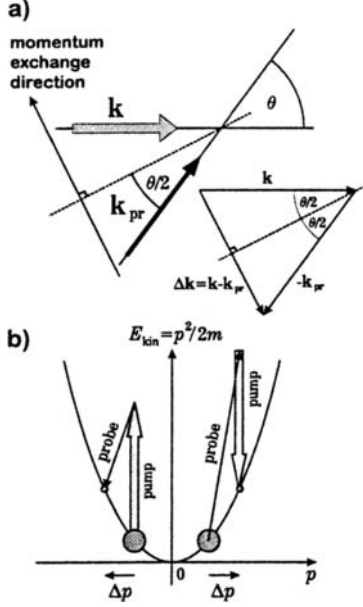
a)

b)

Fig. 7. a) Basic geometry for the recoil induced resonance, associated with atomic interaction with two beams: the pump (thick grey arrow) and probe (thin arrow) beams intersecting in an atomic sample at a small angle θ. b) Raman transitions between the kinetic momentum states for an atom in a state with specific m_g

states, but now we consider the continuum of kinetic momentum states rather than discrete, magnetic sublevels (Fig. 7b),

$$\Delta\Pi\left(p_{\text{final}}, p_{\text{initial}}\right) = \Pi\left(p + \Delta p\right) - \Pi\left(p\right). \tag{5}$$

Integration over all possible momentum values leads to the formula for the RIR signal given as

$$s_{\text{RIR}}(\delta, \theta) = -\int_{-\infty}^{\infty} dp \, \Delta\Pi\left(p_{\text{final}}, p_{\text{initial}}\right) L(\delta). \tag{6}$$

Assuming that $\Pi(p)$ is a Gaussian distribution, $\Delta p \ll p_T = \sqrt{mk_BT}$ and $\gamma \ll kp_T/m$ [5] (all these conditions are fulfilled in our case), one arrives at the analytic formula for the absorption spectrum signal

$$s_{\text{RIR}}(\delta, \theta) = -\sqrt{\frac{m}{2\pi}} \frac{\hbar\delta}{2u_T^{3/2}k\sin\left(\theta/2\right)} \exp\left[-\frac{\delta^2}{2u_T^2(2k\sin(\theta/2))^2}\right], \tag{7}$$

where $u_T = p_T/m$ is the most probable atomic speed. Signal (7) is the derivative of a Gaussian function. It has its minimum/maximum for $\delta = \pm 2u_Tk\sin(\theta/2)$ and the width of the spectrum Δ_{RIR}, defined as the distance between minimum and maximum, is proportional to $\sqrt{T}$. The RIR spectrum can thus serve as a spectroscopic tool for the temperature measurement of a cold atomic sample [5, 23, 24], according to the formula

$$T = \frac{m}{16k_Bk^2\sin(\theta/2)}\Delta_{\text{RIR}}^2. \tag{8}$$

For systems in a thermodynamic equilibrium, T is a well-defined kinetic temperature. If, however, the cold-gas sample is not in thermal equilibrium state, the width of the RIR associated with the momentum transfer in a given direction reflects just the widths of a given component of the momentum distribution [25]. Below, we describe such non-equilibrium situations where the RIR resonances are used to monitor various kinds of the momentum anisotropy. For the sake of simplicity, we characterize the widths of such momentum distributions by quantities of the temperature dimensions bearing, however, in mind these are not properly defined thermodynamical quantities.

The results presented above refer to a two-level atom and a simple pump-probe beam configuration. Nevertheless, this simple approach can be also successfully used in our case in which multilevel atoms are subject to a three dimensional set of trapping beams. Since a distinct RIR contribution appears only near $\delta \approx 0$, it must result from Raman transitions between the momentum states of the same magnetic sublevel, $\Delta m_g = 0$. This implies that our atoms can be effectively treated as two level systems [26,27] and that the polarization of the probe selects the appropriately polarized pump among all six available beams.

For example, consider the case in which the probe beam is σ^--polarized and the quantization axis is parallel to its direction of propagation. Obviously, one contribution to the recoil process is due to the probe beam combined with the nearly co-propagating trapping beam. Analogously, the σ^+-polarized probe interacts with the nearly counter-propagating trapping beam. The second contribution is due to the trapping beams transverse to the probe. In the chosen reference frame, these beams appear as linearly σ and π-polarized. Depending on their relative phases, they represent σ^+- or σ^--polarized pump photons with the same probability, so they equally contribute to the recoil processes both for the σ^+- and σ^--polarized probe. This consideration yields the total RIR signal in the probe beam absorption in the MOT with all six trap beams as equal to

$$s_{\mathrm{RIR,\,MOT}}(\delta) = \begin{cases} s_{\mathrm{RIR}}(\delta, \theta) + 2s_{\mathrm{RIR}}(\delta, 90°) \\ \quad \text{for } \sigma^-\text{-polarized probe,} \\ s_{\mathrm{RIR}}(\delta, 180° - \theta) + 2s_{\mathrm{RIR}}(\delta, 90°) \\ \quad \text{for } \sigma^+\text{-polarized probe.} \end{cases} \tag{9}$$

The above discussion allows one to associate the observed distinct difference between the MOT spectra taken for σ^-- and σ^+-polarized probe exclusively with the recoil processes, since, as it was pointed out in Sec. 3.1, the RZR contributions are insensitive to the probe beam polarization.

3.3. Final modeling of experimental probe absorption spectrum

The considerations presented above lead to the conclusion that both RZR and RIR contribute to the observed spectra, so the complete formula for the absorption signal

becomes

$$s(\delta) = \bar{s}_{\mathrm{RZR}}(\delta) + s_{\mathrm{RIR,MOT}}(\delta)\,, \tag{10}$$

where $\bar{s}_{\mathrm{RZR}}(\delta)$ is the RZR contribution averaged over Rabi frequencies available in a MOT, as discussed in Sec. 3.1. The results of theoretical simulations according to formula (10) are depicted in Fig. 8 (fit $1°$) and compared with experimental data. While the agreement of the modeled and experimental spectra improved considerably after considering both contributions to $s(\delta)$, the theoretical spectrum still exhibits resonances that are too narrow. This indicates that some other kind of inhomogeneous broadening mechanism must affect the spectra. This mechanism is due to the quadrupole MOT magnetic field $\mathbf{B}$ and finite size of the atomic cloud. The results of the theoretical simulation of the absorption spectra with inclusion of the MOT magnetic field are presented in Fig. 8 as fit $2°$ and are compared with the experimental data. In contrast to averaging exclusively over $|\mathbf{E}|$ (fits $0°$ and $1°$), the agreement of the theoretical and experimental absorption signals is now very good.
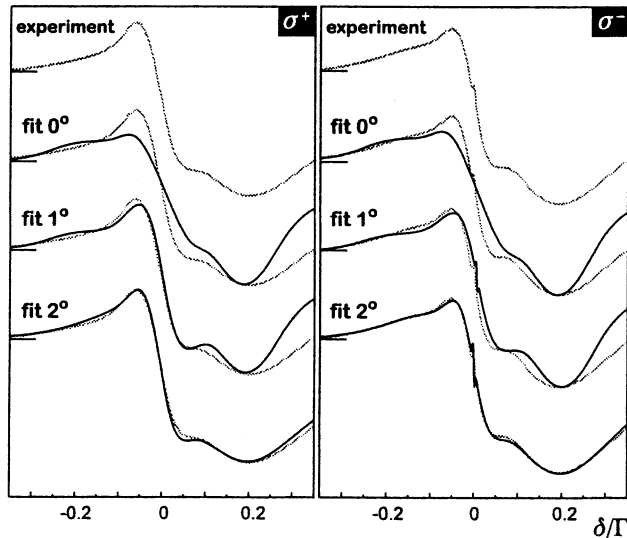

Fig. 8. Experimental and theoretical absorption spectra for σ^+- and σ^--polarized probe beam. The experimental conditions: $I_{\mathrm{max}} = 10.2$ mW/cm^2, $\Delta = -3\Gamma$, $\partial B/\partial z = 13$ G/cm. Fit $0°$ includes only averaging over inhomogeneity of the $\mathbf{E}$ field, fit $1°$ – as fit $0°$ plus RIR, fit $2°$ – as fit $1°$ plus inhomogeneity of the $\mathbf{B}$ field. Parameters of theoretical simulations: Rabi frequency averaging range $\Omega \in [5\Gamma;\ 7.5\Gamma]$; Gaussian width of a single, inhomogeneously broadened resonance $\sigma_B = 0.088\Gamma$, which corresponds to the actual trap size $\sigma_z = 0.9$ mm; the temperature of atomic cloud $T = 155\ \mu$K was fitted to achieve the best agreement of the simulation with experimental data. For better comparison, the experimental spectra are added in grey to each fit

4. Recoil-Induced Resonances: The Tool for Studying Dynamics of Cold Atoms

In the preceding section we discussed two spectral contributions which shape central resonant structure: one due to RZRs and the other due to RIRs. Both stem from Raman transitions induced by trapping light and probe beam photons. However, since the trapping light is neither phase nor intensity stabilized, it is difficult to exploit directly resulting RZRs and RIRs as a systematic diagnostic tool for studying properties of cold atomic sample. The complicated, randomly changing light interference pattern, which results in unstable light polarization and intensity distribution, combined with multilevel structure of the considered transition, precludes the possibility of ruling out the RZRs by systematic fits and hence isolating the RIR contribution for analysis of kinetic properties of the sample.
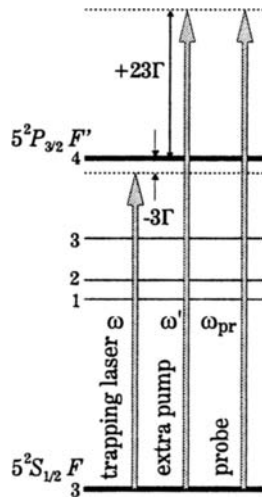

Fig. 9. The laser frequency scheme with an extra, blue-detuned pump for RIR Raman spectroscopy

Rather than attempting to disentangle the RZR and RIR contributions, we have developed a method for observation of a solitary RIR non-overlapping with RZRs. The method is based on introducing an extra pump beam, blue-detuned from the atomic transition by $\delta' \gg \Gamma$ ($+23\Gamma$ in the described experiments) and scanning the probe beam frequency around the frequency of the new pump (Fig. 9). Such a solution has two main advantages. First, it decouples Raman spectroscopy from the not well-controlled trapping field. Second, with the extra pump beam far detuned from atomic resonanceatoms in the trap are only negligibly perturbed, providing the possibility of non-destructive spectroscopic measurement that can be carried out independently from the MOT action. The choice of positive detuning also decreases the influence of other hyperfine transitions. Moreover, the control over polarization of the extra pump, not possible in the case of the trapping field, allows one to choose such a mutual polarization of the pump and probe beams, that only

$\Delta m_F = 0$ Raman transitions are possible. In such a case, the multilevel structure of the ^{85}Rb atom can be effectively treated as a set of independent, two level atoms. It radically simplifies theoretical description of the observed spectra and allows one to use the theory outlined in Sec. 4.

Taking advantage of our new approach to RIR measurement and using different geometry configurations, we were able to measure temperature of MOT as a function of various trapping parameters. the anisotropy of momentum distribution in the unbalanced trap [6] and create and diagnose 1D optical lattices superimposed on the cloud of cold atoms in a working MOT [7]. The next two subsections are devoted to these two latter aspects of application of RIR method to diagnostics of the MOT dynamics.

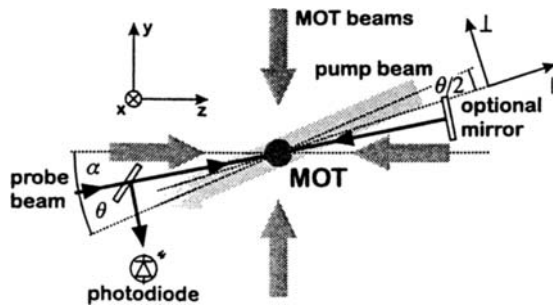## 4.1. Nondestructive study of non-equilibrium states of cold, trapped atoms

Fig. 10. The layout of the experiment. The pump and probe beams intersect in a cloud of cold atoms. With the optional mirror we realize a three-beam configuration in which the momentum exchange is allowed in two directions: $\perp$ and $\parallel$. Third pair of the MOT beams along x and the MOT coils are not shown in this figure

In this part of our experiment, two extra beams intersect in the trap center: the pump and the probe (Fig. 10). The probe beam is directed at a small angle $\alpha = 3°$ to one MOT beam (propagating along z), and the pump is at $\theta = 5°$ to the probe. The probe beam can be detected either directly or after retroreflection from the optional mirror. The setup with the retroreflected probe enables the measurement of the momentum distribution $\Pi(p)$ simultaneously along two perpendicular directions: $\perp$, for angle θ between the pump and the nearly co-propagating probe, and $\parallel$, for angle $180° - \theta$ between the pump and the nearly counter-propagating probe. When α and θ are sufficiently small, $\perp$ and $\parallel$ almost coincide with the y and z directions, respectively. Both pump and probe beams are derived from diode lasers synchronized by injection-locking to the same master laser and are blue-detuned from the trapping transition $^2S_{1/2}(F = 3)$-$^2P_{3/2}(F' = 4)$ by $\Delta = 2\pi\cdot140$ MHz

$\approx 23\,\Gamma$, where Γ denotes the natural linewidth. As mentioned before, such big detuning reduces the perturbation of atoms to a very low level (scattering rate $\propto 1/\Delta^2$) which is essential for non-destructive measurements. Despite large Δ, the pump and probe beams drive the Raman signal with a sufficiently large amplitude and signal-to-noise ratio for the pump beam intensities 5–35 mW/cm^2.

The probe beam is scanned by $\delta \approx \pm 1$ MHz around frequency ω' of the pump. The probe and pump photons induce Raman transitions between atomic kinetic states separated by $\pm \hbar \delta$. Since the polarization of the pump and probe beams is chosen to be the same, the atoms undergo Raman transitions with $\Delta m_F = 0$. Hence, the internal atomic state does not change and the only states that have to be considered are the external states associated with the kinetic energy of the atomic center-of-mass. With the assumption that $\Pi(\mathbf{p})$ is the Maxwell–Boltzmann distribution, the RIR signal $s(\delta)$ recorded with the retroreflected probe is given by two contributions. The narrow one results from the Raman process involving the pump and the probe beam making small angle θ and the wide one is for angle $180° - \theta$. The signal is

$$s(\delta) \propto -A_\perp \delta \exp\left(-\frac{\delta^2}{\xi_\perp^2}\right) - A_{||}\delta \exp\left(-\frac{(\delta - \delta_0)^2}{\xi_{||}^2}\right), \qquad (11)$$

where, for small θ, $\xi_\perp^2 \approx 2k_B k^2 m^{-1}\theta^2 \tau_\perp$ and $\xi_{||}^2 \approx 8k_B k^2 m^{-1}\tau_{||}$. $\tau_\perp$ and $\tau_{||}$ are the distribution widths in the $\perp$ and $||$ directions in the temperature units, $A_{||}$ and $A_\perp$ are the amplitudes of the corresponding contributions, m is the atomic mass, k_B is the Boltzmann constant, and δ_0 is the possible frequency shift between the $\perp$ and $||$ contributions, to be discussed later.

Typical example of the retroreflected-probe transmission spectrum is shown in Fig. 11. It exhibits two distinct resonant contributions, predicted by Eq. (11). The wide contribution is shifted with respect to the narrow one by 72.4 kHz, which indicates a 2.8-cm/s average velocity component in the $||$ direction. We thus observe an atomic drift within a cloud, which as a whole remains stationary. We understand this as a dynamic effect resulting from a small difference of the radiation pressures intrinsic to a MOT with retroreflected trapping beams. Indeed, the observed shift increases when the imbalance is purposely increased. Strong imbalance normally produces a displacement of the atomic-cloud center of mass. In our case this displacement is too weak to be detected by standard imaging technique, while the anisotropic atomic flow, even one order of magnitude slower than the mean thermal velocity, is well measurable with our method.

As the velocity distributions derived from the signal in Fig. 11 are Gaussian, one can determine the values $\tau_\perp = 172 \pm 6\,\mu$K and $\tau_{||} = 170 \pm 3\,\mu$K. The equality of these τs implies thermodynamical equilibrium and allows their interpretation as temperature T, despite the slow drift. The equilibrium persists for various MOT-light intensities due to the fact that total intensities of each pair of the MOT beams remain the same. The observed nearly linear increase of T with the total MOT-beam intensity agrees well with previous reports [28–30].
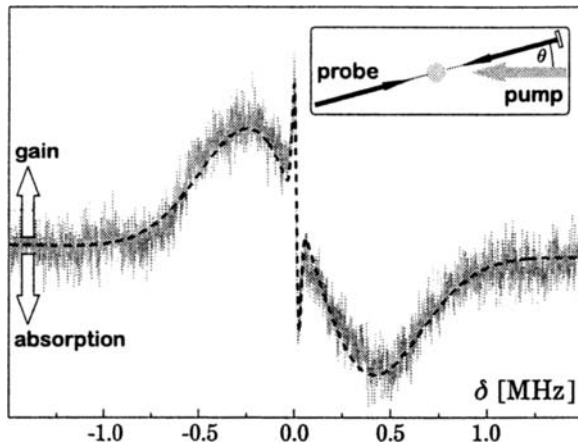
Fig. 11. Transmission spectrum of a retroreflected probe (gray) and the theoretical prediction (dashed) of Eq. (11). Inset: the beam setup. The MOT beams have intensities $I_{\mathrm{MOT}} = 13.8 \ \mathrm{mW/cm^2}$ per beam and are detuned from the trapping transition by $\Delta_{\mathrm{MOT}} = -3\,\Gamma$, the repumper beam intensity $I_{\mathrm{REP}} = 15 \ \mathrm{mW/cm^2}$, the axial magnetic field gradient $\partial_x B = 12$ Gauss/cm, the pump beam intensity $I = 33 \ \mathrm{mW/cm^2}$, and the probe beam intensity $0.3 \ \mathrm{mW/cm^2}$. A week imbalance of the retroreflected trapping beam intensities is responsible for the visible shift of the narrow and wide resonance centers (see text)

The thermodynamics of the system becomes highly non-trivial when the trapping light is unevenly distributed between the MOT beam pairs. It was predicted that for such conditions the width of kinetic momentum distribution shows directional dependence [31]. Using the simultaneous measurement of the momentum width in two perpendicular directions, we attempted to observe such anisotropic non-equilibrium state of the cold-atom cloud. For this reason, we changed intensity balance between the longitudinal (I_z) and transverse (I_x, I_y) MOT beam pairs, while keeping the total intensity $I_0 = I_x + I_y + I_z$ constant. We define parameter κ as the relative intensity of I_z, $I_z = \kappa I_0$, $I_x = I_y = (1 - \kappa)I_0/2$. The results of the measurement of $\tau_{\parallel}$ and $\tau_{\perp}$ for different values of κ are depicted in Fig. 12. For equal partition of the trapping intensity ($\kappa = 1/3$), the widths of kinetic momentum distributions are the same, as expected. However, when κ increases, $\tau_{\parallel}$ and $\tau_{\perp}$ follow opposite trends, which is evidence of a kinetic momentum anisotropy in a MOT working MOT and thereby its non-equilibrium state. A similar anisotropy was recently observed also in an optically dense sample [32]. We notice that $\tau_{\parallel} + 2\tau_{\perp}$, which is the measure of $v_{\parallel}^2 + 2v_{\perp}^2$, is constant within $\pm 2\%$ over the whole measured range of κ. The decrease of $\tau_{\parallel}$ with the growing κ is due to the fact that the heating associated with spontaneous emission is isotropic, whereas the cooling rate is higher for the direction with the increased intensity. The momentum anisotropy becomes manifest because the density of the atoms is too small to provide efficient ther-

malization. Indeed, simple estimation for typical conditions and Rb–Rb collision cross-section $\sigma_{Rb-Rb} = 3 \cdot 10^{-13}$ cm^2 [33] yields the atomic collision rate below 1 Hz in our trap, while the friction coefficient, in frequency units, is in the kHz range.
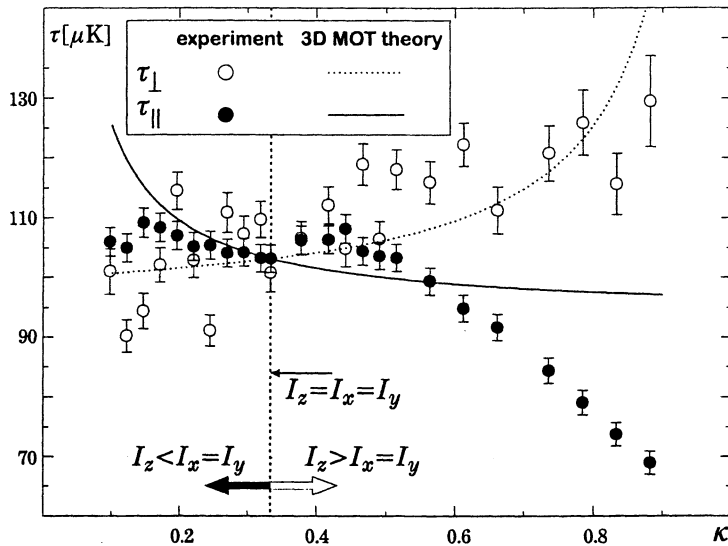

Fig. 12. Widths of the kinetic momentum distributions (in μK units) measured as a function of relative intensity κ in the two perpendicular directions, $\tau_\perp$ (hollow circles)and $\tau_{||}$ (filled circles). For the equilibrium ($\kappa = 1/3$), $I_{MOT} = 6.8$ mW/cm^2, $\tau_\perp = 100 \pm 3$ μK, and $\tau_{||} = 103 \pm 2$ μK. Other parameters as in Fig. 11. Theoretical curves are plotted according to Refs. [31,34]

The theoretical behavior of $\tau_{||}$ and $\tau_\perp$ according to Refs. [31,34] is plotted in Fig. 12 along with the experimental data. They exhibit similar qualitative dependence (the decrease of $\tau_{||}$ and the increase of $\tau_\perp$ with growing κ), but the existing theory fails to reproduce the exact shape of the experimental dependence. This discrepancy is due to additional mechanism of sub-Doppler cooling, not included in the calculations of Ref. [31]. Indeed, the increase of I_z accompanied by attenuation of I_x and I_y results in efficient quasi-1D cooling scheme in the $\sigma^+ - \sigma^-$ optical molasses [35]. Evidence of this cooling is provided by the values of $\tau_{||}$ falling to 70 μK, well below the Doppler cooling limit of 140 μK. Importance of sub-Doppler cooling for anisotropy of momentum distribution in cold atomic samples has been previously noted in optical molasses [36].

4.2. 1D optical lattice in a MOT diagnosed by recoil-induced resonances

In the previous subsection we discussed the experimental setup where the probe beam was recorded after retroreflection. Such a configuration enables simultaneous

measurement of momentum distribution in two orthogonal directions. However, there is another option of accessing such a possibility. Instead of retroreflecting the probe beam, one can reflect the extra pump beam, as depicted if Fig. 13. In such a configuration, there are also two different angles between probe and one of the pump beams, θ and $180° - \theta$ and, consequently, two directions of the possible momentum transfer.

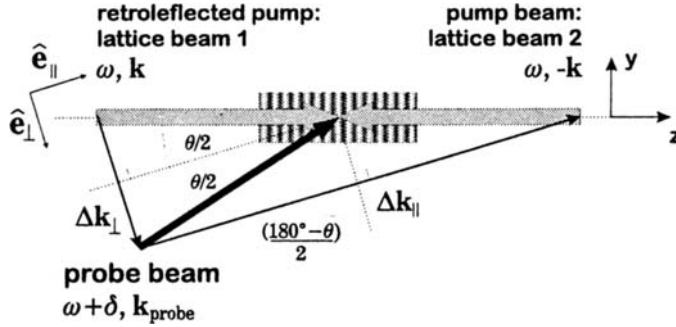**Fig. 13.** Geometry of the light beams used for creation and diagnostics of 1D optical lattice in a MOT, and momentum transfers $\hbar\Delta\mathbf{k}_{\parallel}$ and $\hbar\Delta\mathbf{k}_{\perp}$ in the resulting Raman transitions

However, in contrast to the case discussed in Sect. 4.1, the intense retroreflected pump beam constitutes a standing wave with a modulated-intensity pattern which serves as an 1D optical lattice for the atoms. As a result the atomic motion in one direction becomes restricted to the potential wells of the size of $\lambda/2$ and hence quantized. This results in vibrational structure of energy levels, unevenly spaced by $\hbar\omega_v^{(1)}$, $\hbar\omega_v^{(2)}$, ..., which differ because of anharmonicity of the potential (Fig. 14). By averaging the vibrational level spacing over anharmonicity with weights reflecting the temperature-dependent populations of given vibrational levels one can find
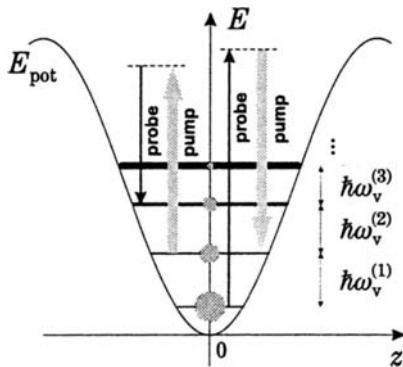

Fig. 14. Raman transitions between vibrational levels of atoms bound in the optical lattice potential. The vibrational level spacing decreases due to anharmonicity. The sizes of circles symbolize populations of the relevant levels

positions of the most distinct Raman vibrational resonances [8,37]. The first harmonic, $\delta = \pm\bar{\omega}_v^I$, and overtone, $\delta = \pm\bar{\omega}_v^{II}$, are associated with the change of vibrational quantum numbers by one and two, respectively. Atoms trapped in the lattice do not give rise to the wide RIR signal associated with movement in the $\hat{e}_{||}$ direction. They participate only in the generation of narrow RIR and Raman vibrational spectrum. Such a suppression of recoil in an optical lattice, consistent with the previous predictions [20,38–40] and experiments [8,41] suggests a novel method for diagnostics of lattice loading by measuring the magnitude of the appropriate RIR signal.

Various kinds of pump-probe spectra discussed in this section are illustrated in Figs. 15a, 15b with the results of our experiments. All measured signals are fitted with the formula

$$s(\delta) = - A_{||} \frac{\partial \mathcal{G}(\delta, \xi_{||})}{\partial \delta} - A_\perp \frac{\partial \mathcal{G}(\delta, \xi_\perp)}{\partial \delta}$$
$$+ L_I \left[\mathcal{L}(\delta, -\bar{\omega}_v^I, \gamma^I) - \mathcal{L}(\delta, \bar{\omega}_v^I, \gamma^I) \right] \qquad (12)$$
$$+ L_{II} \left[\mathcal{L}(\delta, -\bar{\omega}_v^{II}, \gamma^{II}) - \mathcal{L}(\delta, \bar{\omega}_v^{II}, \gamma^{II}) \right],$$

where $\mathcal{G}(\delta, \xi)$ is the normalized Gaussian describing kinetic momentum distribution of width ξ, and $\mathcal{L}(\delta, \omega, \gamma)$ is the Lorentzian used for modeling the Raman vibrational resonance of width γ centered at ω; $A_{||}$ and $A_\perp$ represent amplitudes of the wide ($||$) and narrow ($\perp$) RIR contributions, and L_I and L_{II} are the amplitudes of the vibrational resonances associated with the first harmonic at $\bar{\omega}_v^I$ and overtone at
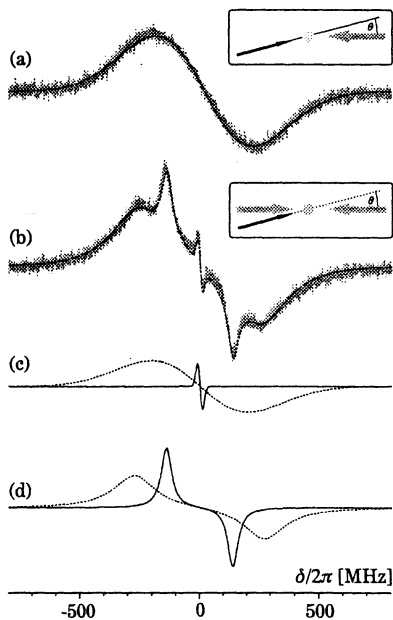

Fig. 15. Experimental spectra recorded at $T = 64\ \mu K$ and the corresponding fits. (a) Single, wide RIR spectrum (grey) acquired in the simple two-beam configuration shown in the inset. Dotted black line represents the fit by the first term of Eq. (12). Such spectra are used to determine temperature of the atomic cloud. (b) Experimental spectrum (grey) recorded in the presence of the 1D optical lattice (inset) and the fit by all terms of Eq. (12) (black). (c) RIR components of the fit: wide RIR associated with the momentum exchange in the $||$ direction (dotted line) and narrow RIR associated with the exchange in the $\perp$ direction (solid line). (d) Vibrational components: first harmonic (solid line) and overtone (dotted line), extracted from the fit

$\bar{\omega}_v^{\prime\prime}$, respectively. Figs. 15c, 15d show isolated recoil and vibrational contributions of expression (12) to the spectrum of Fig. 15b. In principle, in addition to the discussed RIR and vibrational transitions, elastic transitions with $\delta = 0$ are possible both in optical lattice and for free atoms. However, as shown in Refs. [38–40], the resulting Rayleigh elastic scattering contribution is negligibly small in our geometry and polarization configuration.
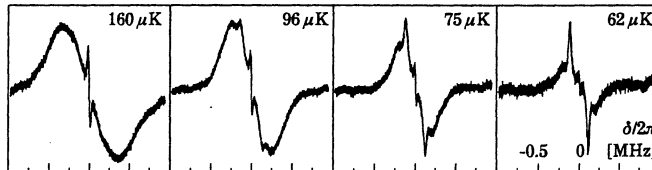

Fig. 16. Comparison of the probe transmission spectra for various MOT-beam temperatures. For sufficiently low temperatures the wide RIR contribution disappears while the lattice contribution becomes distinct. The sequence of spectra illustrates well the competition between the free and bound atoms. Vertical scale is the same for all plots

Figure 16 presents the series of measurements taken for different temperatures of the atomic cloud. The temperature is controlled by the MOT beam intensity and is determined by the width of the wide RIR. At temperatures below about the Doppler limit, $T_D = 140$ μK, atoms localized in lattice wells become a significant fraction of the whole sample and give rise to a pronounced vibrational structure.

In the spectra measured with three-beam configuration the first vibrational component is very distinct but the overtone overlaps with the wide RIR, which greatly obstructs interpretation of the lattice spectra. This obstacle can be removed by a thorough separation of RIR and lattice contributions. For this sake, we reduced the number of free parameters by determining the temperature of the cold atomic cloud for each measurement. This was done by blocking the mirror that retroreflects the lattice beam (Fig. 13) and by performing two-beam RIR velocimetry with nearly counter-propagating Raman beams [6, 23]. In such a configuration, the only contribution to the spectrum is the RIR associated with the momentum transfer along the $\hat{e}_{||}$ direction (Fig. 15a). Since our 1D optical lattice does not exhibit spatial polarization modulation, no additional cooling mechanism is present. This allows us to assume that the temperature of atoms in a MOT with and without the lattice is the same. Having determined the width $\xi_{||}$, we calculated the temperature T and the width $\xi_\perp = \xi_{||} \tan(\theta/2)$ [3, 6]. Next, the widths $\xi_{||}$ and $\xi_\perp$ were used as constants in the first terms of the fit given by Eq. (12) and then the fitted RIR contributions were subtracted from the spectra recorded with both lattice beams. The resulting difference constitutes pure lattice contribution which is very well reproduced by the last terms of Eq. (12), as seen in Fig. 17.

For decreasing temperature of the atomic cloud, we observed increase of the amplitude of the vibrational contribution relative to the RIR contribution. This in-
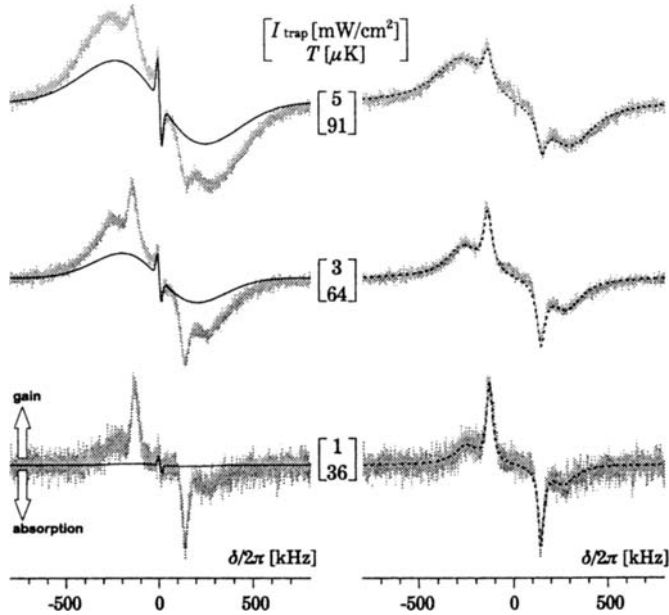
Fig. 17. Probe transmission spectra with 1D optical lattice recorded for various MOT-beam intensities and related temperatures. Left column, measured spectra (grey) and RIR contributions (solid black) determined from two-beam thermometry (see text). Right column, vibrational contributions extracted by subtraction of RIR components from full spectra and theoretical fits (dotted). The vertical scale is the same for all plots

dicates a growth of the fraction localized in the 1D optical lattice. We also observed systematic variation of the relative amplitudes of the two RIR contributions. As it can be seen in Fig. 17, for lower temperatures the amplitude of the wide RIR associated with the momentum exchange in the ∥ direction is noticeably smaller than the amplitude of the narrow RIR determined by the exchange in the ⊥ direction. This behavior can be explained by constraints imposed by the 1D optical lattice on the atomic movement resulting in suppression of the recoil in the ∥ direction. Hence, localized atoms do not contribute to the wide RIR. Since the increase of the lattice-trapped fraction caused by the temperature lowering proceeds at the expense of unbound atoms, the amplitude of the wide RIR becomes smaller. Inversely, since there is no lattice trapping in the ⊥ direction, the localization does not affect the narrow RIR, the amplitude of which depends only on the total number of atoms. Further lowering of the temperature leads to the complete suppression of the wide RIR, which indicates that all atoms still remaining in a MOT are loaded into 1D optical lattice. This qualitative consideration suggest the way of controlling the ratio of the lattice-localized to unbound atoms.
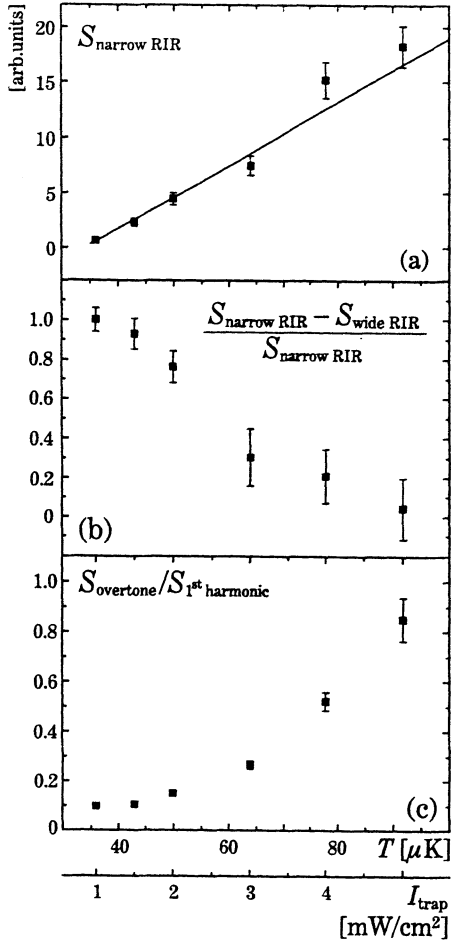
Fig. 18. Trap-beam intensity and temperature dependence of the atomic fractions estimated by calculating areas S associated with relevant spectra contributions: (a) $S_{\text{narrow RIR}}$, re-scaled as described in text, proportional to the total number of atoms in a MOT, (b) $(S_{\text{narrow RIR}} - S_{\text{wide RIR}})/S_{\text{narrow RIR}}$, the atomic fraction localized in a 1D optical lattice, (c) $S_{\text{overtone}}/S_{\text{1st harmonic}}$, the ratio of atoms undergoing Raman transitions responsible for the 1st harmonic and overtone

To examine the behavior of the discussed atomic fractions quantitatively, we numerically estimated the number of atoms which give rise to the relevant terms of Eq. (12). Since RIR signals are proportional to derivative of atomic momentum distributions, we first reconstructed their integrals and then evaluated the areas under resulting curves. In case of lattice contributions we calculated the areas directly under the vibrational Raman signals.

Figure 18a presents the area $S_{\text{narrow RIR}}$ as a function of MOT temperature. $S_{\text{narrow RIR}}$ is obtained by calculating the area under momentum distribution derived from the first term of Eq. (12) and dividing by the geometrical factor $\tan^2(\theta/2)$ [3, 6] for comparison with $S_{\text{wide RIR}}$, the area associated with the second term of Eq. (12). Since there is no lattice trapping in this direction, $S_{\text{narrow RIR}}$ is proportional to the total number of atoms in the trap. In consistency with previous observations [42] it decreases linearly when MOT-beam intensity is lowered.

Figure 18b depicts the ratio $(S_{\text{narrow RIR}} - S_{\text{wide RIR}})/S_{\text{narrow RIR}}$ which, due to the same transition amplitudes for both RIRs, is a direct measure of the fraction captured by 1D optical lattice. As expected, the localized fraction grows with decreasing temperature. For the temperature of 30 μK all the MOT-trapped atoms are in the optical lattice. The absolute number of atoms localized in the lattice also begins to grow with decreasing temperature, but then the general decrease of the total number of atoms in the MOT prevails. The number of atoms in the lattice reaches its maximum at about 60 μK when the captured fraction is close to 0.5.

For growing temperatures we observed a systematic increase of the overtone contribution relative to the 1st harmonic ($S_{\text{overtone}}/S_{\text{1st harmonic}}$ ratio, depicted in Fig. 18c). The rising probability of the overtone transitions is attributed to the fact that for higher temperature population is shifted towards higher vibrational levels with more pronounced anharmonicity [43].

5. Conclusions

We have successfully explained absorption spectra recorded in a working MOT and identified various processes responsible for the resonance features observed in the different probe-tuning range. We have shown that full agreement between the theory and experimental data is attainable only when realistic MOT conditions, the light and the magnetic field inhomogeneities are taken into account. Our theoretical analysis emphasized the importance of the atomic recoil processes in a MOT which led us to its using in the novel approach to the diagnostics of the dynamics of cold atomic sample.

We have developed novel three-beam spectroscopic method of determining the momentum distributions, which is non-destructive, highly sensitive and provides multi-dimensional momentum determination in a single measurement. Its potential has been demonstrated by our study of three different momentum distributions of atoms in the operating magneto-optical trap: i) thermodynamic equilibrium with well defined temperature and Gaussian momentum distribution with a slow velocity drift; ii) non-equilibrium state characterized by Gaussian distributions with drastically different widths in the longitudinal and transverse directions. The described method can be also straightforwardly applied to 3D case by introducing additional pump beam in the xz plane in Fig. 10.

We have also performed pump-probe spectroscopy of ^{85}Rb atoms in an operating MOT equipped with an extra pair of lattice beams. Application of a simple 1D lattice of a standing-wave configuration and nondestructive RIR thermometry allowed studies of the localization efficiency at well-determined atomic temperature, not affected by the lattice. The recorded pump-probe spectra revealed complex structure composed of the recoil-induced and vibrational resonances due to the free, and lattice-bound atoms, respectively. We have shown how to resolve the pump-probe spectra for an atomic system consisting of two atomic fractions and applied this technique to the spectra taken at various atomic temperatures. This extension of a standard RIR velocimetry proved very useful for nondestructive di-

agnostics of 1D-lattice loading. We were able to verify that the creation of a robust 1D optical lattice is possible by loading of relatively hot ($\sim$100 μK) atoms directly from a continuously operating regular MOT without any further cooling.

Acknowledgments

References

1. B. Lounis, J. Courtois, P. Verkerk, C. Salomon and G. Grynberg, *Phys. Rev. Lett.* **69** (1992) 3029.
2. D. Grison, B. Lounis, C. Salomon, J.Y. Courtois and G. Grynberg, *Europhys. Lett.* **15** (1991) 149.
3. T.M. Brzozowski, M. Brzozowska, J. Zachorowski, M. Zawada and W. Gawlik, *Phys. Rev. A* **71** (2005) 013401.
4. see, e.g., G. Grynberg and C. Robilliard, *Phys. Rep.* **355** (2001) 335 and references therein.
5. G. Grynberg. J.-Y. Courtois, B. Lounis and P. Verkerk, *Phys. Rev. Lett.* **72** (1994) 3017.
6. M. Brzozowska, T.M. Brzozowski, J. Zachorowski and W. Gawlik, *Phys. Rev. A* **72** (2005) 061401(R).
7. M. Brzozowska, T.M. Brzozowski, J. Zachorowski and W. Gawlik, *Phys. Rev. A* **73** (2006) 063414.
8. P. Verkerk, B. Lounis, C. Salomon, C. Cohen-Tannoudji and J. Courtois, *Phys. Rev. Lett.* **68** (1992) 3861.
9. Y.-C. Chen, Y.-W. Chen, J.-J. Su, J.-Y. Huang and I.A. Yu, *Phys. Rev. A* **63** (2001) 043808.
10. G.C. Cardoso, J.W.R. Tabosa, *Opt. Comm.* **185** (2000) 353.
11. A. Hemmerich, M. Weidemller, T. Esslinger and T.W. Hnsch, *Europhys. Lett.* **21** (1993) 445.
12. J.W.R. Tabosa, G. Chen, Z. Hu, R.B. Lee and H.J. Kimble, *Phys. Rev. Lett.* **66** (1991) 3245.
13. H. Schadwinkel, U. Reiter, V. Gomer and D. Meschede, *Phys. Rev. A* **61** (1999) 013409.
14. J. Zachorowski, T. Pałasz and W. Gawlik, *Optica Applicata* **28** (1998) 239.
15. see, e.g., R.W. Boyd, *Nonlinear Optics*, Academic Press, Inc., Boston, 1992.
16. C. Cohen-Tannoudji, *Atoms in Strong Resonant Fields*, Frontiers in Laser Spectroscopy, eds. R. Balian and S. Haroche and S. Liberman, Les Houches Session XXVII, July 1975, p. 1, North-Holland, Amsterdam, 1977.
17. J.-Y. Courtois and G. Grynberg, *Phys. Rev. A* **46** (1992) 7060.
18. S.A. Hopkins and A.V. Durrant, *Phys. Rev. A* **56** (1997) 4012.

19. J. Zachorowski, T. Brzozowski, T. Pałasz, M. Zawada and W. Gawlik, *Acta Phys. Polon. A* **101** (2002) 61.

20. J. Guo, P.R. Berman, B. Dubetsky and G. Grynberg, *Phys. Rev. A* **46** (1992) 1426.

21. M.C. Fischer, A.M. Dudarev, B. Gutiérrez-Medina and M.G. Raizen, *J. Opt. B: Quantum Semiclass. Opt.* **3** (2001) 279.

22. P. Verkerk, *Proc. Intern. School of Physics*, Varenna, Course **CXXXI** (1996) p. 325.

23. D.R. Meacher, D. Boiron, H. Metcalf, C. Salomon and G. Grynberg, *Phys. Rev. A* **50** (1994) R1992.

24. G. Di Domenico, G. Mileti and P. Thomann, *Phys. Rev. A* **64** (2001) 043408-1.

25. In some situations, for example when momentum distribution is asymmetric, its width cannot be properly defined. We have observed such distributions in our experiment when the trapping beams were not accurately aligned and their detuning from atomic resonant frequency was decreased [6].

26. A. Lezama, G.C. Cardoso and J.W.R. Tabosa, *Phys. Rev. A* **63** (2001) 013805.

27. A. Lipsich, S. Barreiro, A.M. Akulshin and A. Lezama, *Phys. Rev. A* **61** (2000) 053803.

28. P.D. Lett, W.D. Phillips, S.L. Rolston, C.E. Tanner, R.N. Watts, C.I. Westbrook, *J. Opt. Soc. Am. B* **6** (1989) 2085.

29. C.D. Wallace, T.P. Dinneen, K.Y.N. Tan, A. Kumarakrishan, P.L. Gould and J. Javanainen, *J. Opt. Soc. Am. B* **11** (1994) 703.

30. X. Xu, T.H. Loftus, M.J. Smith, J.L. Hall, A. Gallagher and J. Ye, *Phys. Rev. A* **66** (2002) 011401(R).

31. M. Gajda and J. Mostowski, *Phys. Rev. A* **49** (1994) 4864.

32. A. Vorozcovs, M. Weel, S. Beattie, S. Cauchi and A. Kumarakrishnan, *J. Opt. Soc. Am. B* **22** (2005) 943.

33. U.D. Rapol and A. Wasan and V. Natarajan, *Phys. Rev. A* **64** (2001) 023402.

34. M. Gajda, private communication.

35. J. Dalibard and C. Cohen-Tannoudji, *J. Opt. Soc. Am. B* **6** (1998) 2023.

36. J. Javanainen, *Phys. Rev. A* **46** (1992) 5819; J. Javanainen, *J. Phys. B: At. Mol. Phys.* **27** (1994) L41; Y. Castin and K. Mølmer, *Phys. Rev. Lett.* **74** (1995) 3772.

37. P.S. Jessen, C. Gerz, P.D. Lett, W.D. Phillips, S.L. Rolston, R.J.C. Spreeuw and C.I. Westbrook, *Phys. Rev. Lett.* **69** (1992) 49.

38. J. Guo and P. Berman, *Phys. Rev. A* **47** (1993) 4128.

39. J. Guo, *Phys. Rev. A* **49** (1994) 3934.

40. J. Guo, *Phys. Rev. A* **52** (1995) 1458.

41. A. Hemmerich and T.W. Hänsch, *Phys. Rev. Lett.* **70** (1993) 410.

42. see, e.g., K. Lindquist, M. Stephens and C. Wieman, *Phys. Rev. A* **46** (1992) 4082.

43. G. Herzberg, *Molecular Spectra and Molecular Structure*, Krieger Publishing Co., Melbourne, FL, 1992, pp. 85–88.